BLOCH THEORY-BASED GRADIENT RECOVERY METHOD FOR COMPUTING TOPOLOGICAL EDGE MODES IN PHOTONIC GRAPHENE

HAILONG GUO*, XU YANG†, AND YI ZHU‡

Abstract. Photonic graphene, a photonic crystal with honeycomb structures, has been intensively studied in both theoretical and applied fields. Similar to graphene which admits Dirac Fermions and topological edge states, photonic graphene supports novel and subtle propagating modes (edge modes) of electromagnetic waves. These modes have wide applications in many optical systems. In this paper, we propose a novel gradient recovery method based on Bloch theory for the computation of topological edge modes in the honeycomb structure. Compared to standard finite element methods, this method provides higher order accuracy with the help of gradient recovery technique. This high order accuracy is highly desired for constructing the propagating electromagnetic modes in applications. We analyze the accuracy and prove the superconvergence of this method. Numerical examples are presented to show the efficiency by computing the edge mode for the $\mathcal{P}$-symmetry and $\mathcal{C}$-symmetry breaking cases in honeycomb structures.

AMS subject classifications.

Key words. Gradient recovery, superconvergence, edge mode, honeycomb structure, topological photonics

1. Introduction.

Graphene has been one of the popular research topics in different theoretical and applied fields in the past two decades [12]. Its success inspires a lot of analogs (referred to as "artificial graphene") which are two-dimensional systems with similar properties to graphene [17, 22, 27, 28, 31, 32]. Among these analogs, Photonic graphene, a photonic crystal with honeycomb structures, has attracted a lot of interest recently [1, 26, 27]. Similar to graphene which admits Dirac Fermions and topological edge states, photonic graphene supports novel and subtle propagating localized modes of electromagnetic waves. These modes are the main research objects in topological photonics and have large applications in many optical systems [20, 21], and thus it is crucial to understand such interesting propagating modes. This brings opportunities and challenges to both applied and computational mathematics.

The propagation of electromagnetic waves in media is governed by the Maxwell equations in three spatial dimensions. Thanks to the symmetries of photonic crystals, the in-plane propagation of electromagnetic waves can be reduced to the following eigenvalue problem in $L^2(\mathbb{R}^2)$ [18],

$$\mathcal{L}^W \Psi \equiv -\nabla \cdot W(\mathbf{x}) \nabla \Psi = E\Psi, \quad \mathbf{x} \in \mathbb{R}^2. \tag{1.1}$$

Physically, $\Psi(\mathbf{x})$ represents the propagating mode of electromagnetic waves, the eigenvalue E is related to the frequency of the wave, and the positive definite Hermitian matrix function $W(\mathbf{x})$ corresponds to the material weight of the media; see [18] for details.

*Department of Mathematics, University of California, Santa Barbara, CA, 93106, USA (hlguo@math.ucsb.edu).

†Department of Mathematics, University of California, Santa Barbara, CA, 93106, USA (xuyang@math.ucsb.edu). This work was partially supported by the NSF grant DMS-1418936.

‡Zhou Pei-Yuan Center for Applied Mathematics, Tsinghua University, Beijing, 100084, People's Republic of China (yizhu@mail.tsinghua.edu.cn). This work was partially supported by Tsinghua University Initiative Scientific Research Program (Grant 20151080424)

If the medium is a perfect photonic crystal, the material weight $W(\mathbf{x})$ is periodic. In applications, a bulk photonic crystal is often modulated by different types of defects which break the periodicity of the medium. For instance, in this work, we will consider a photonic graphene modulated by a domain wall defect. Under proper assumptions on $W(\mathbf{x})$, properties of electromagnetic modes in photonic graphene can be analyzed, for example, in [18], however, in general one needs to resort to numerical computation to investigate the existence and study the properties of electromagnetic modes.

The numerical challenge of the eigenvalue problem (1.1) in photonic lattice lies in the lattice structure. For bulk geometry, $W(\mathbf{x})$ is periodic and the eigenfunction Ψ is semi-periodic (periodic up to a phase) in each lattice, and thus spectral method can not be directly applied unless one applies the Bloch theory first [6]. However, when one introduces the domain-wall modulated defect to break the symmetry of geometry which leads to the appearance of edge modes, the spectral method no longer works due to the loss of symmetry and semi-periodic boundary conditions in the lattice. Since $\mathcal{L}^W$ has a divergence form, finite element method comes to be a natural choice. In applications, it is also very important to accurately compute the mode $\Psi(\mathbf{x})$ and its gradient in order to construct the full electromagnetic fields under propagation [18], and therefore a finite element method with high order accuracy in gradient is desired for the computation of (1.1).

Gradient recovery methods are one of the major postprocessing techniques based on finite element methods, which are able to provide superconvergent gradient and asymptotically exact *a posteriori* error estimators [2, 5, 7, 23, 34–36], anisotropic mesh adaption [10, 11, 16], and enhancement of eigenvalue approximation [14, 25, 30]. Recently, recovery techniques are used to construct new finite element methods for higher order partial differential equations [8, 15]. A famous example of gradient recovery methods is the Superconvergent Patch Recovery (SPR) proposed by Zienkiewicz and Zhu [35], also known as ZZ estimator, which has become a standard tool in many commercial Finite Element software such as ANSYS, Abaqus, and LS-DYNA. An important alternative is the polynomial preserving recovery (PPR) proposed by Zhang and Naga [33], which improved the performance of SPR on chevron pattern uniform mesh. It has also been implemented by commercial Finite Element software COMSOL Multiphysics as a superconvergence tool. However, direct application of gradient recovery methods to (1.1) leads to huge computational cost due to the existence of lattice structure.

In this paper, we consider the honeycomb lattice structure and develop a gradient recovery method based on Bloch theory. We apply the Bloch theory in the direction that has no domain-wall modulated defect, and then use the gradient recovery method to solve the eigenvalue problem for each wave number. Compared to standard finite element methods, this method provides higher order accuracy with the help of gradient recovery technique. We analyze the accuracy and prove the superconvergence of this method. We also compute the edge modes for the $\mathcal{P}$-symmetry and $\mathcal{C}$-symmetry breaking cases in honeycomb structures to show the efficiency of the method. Our results are consistent with the analytical results given in [18].

The rest of the paper is organized as follows. In Section 2, we introduce the problem background on photonic graphene, Dirac points and edge modes and the Bloch-Floquet theory; In Section 3, we propose the gradient recovery method based on Bloch theory, analyze the accuracy and prove the superconvergence of the method; numerical examples of computing $\mathcal{P}$-symmetry and $\mathcal{C}$-symmetry breaking cases in honeycomb structures are presented in Section 4 to show the efficiency, and we give

conclusive remarks in Section 5.

2. Preliminary. In this section, we summarize basic properties of the photonic graphene, Dirac points and edge states as a description of problem background, and refer interested readers to [18] and references therein for more details.

2.1. Honeycomb-structured material weight. A perfect photonic graphene has a honeycomb structured material weight, *i.e.*, $W(\mathbf{x}) = A(\mathbf{x})$, with the honeycomb structured material weight $A(\mathbf{x})$ mathematically satisfies

1. $A(\mathbf{x})$ is Hermitian, positive definite, bounded away from zero and infinity;
2. $A(\mathbf{x}+\mathbf{v}) = A(\mathbf{x})$ for all $\mathbf{x} \in \mathbb{R}^2$ and $\mathbf{v} \in \Lambda_h$;
3. $\overline{A(-\mathbf{x})} = A(\mathbf{x})$; ($\mathcal{PC}$-invariance)
4. $A(R^*\mathbf{x}) = R^* A(\mathbf{x}) R$; ($\mathcal{R}$-invariance)

Here, the honeycomb lattice Λ_h is a hexagonal lattice generated by, e.g.,

$$\mathbf{v}_1 = \begin{pmatrix} \frac{\sqrt{3}}{2} \\ \\ \frac{1}{2} \end{pmatrix}, \quad \mathbf{v}_2 = \begin{pmatrix} \frac{\sqrt{3}}{2} \\ \\ -\frac{1}{2} \end{pmatrix};$$

$\mathbf{x} \mapsto R\mathbf{x}$ is the mapping on $\mathbb{R}^2$ which rotates a vector clockwise by 120° ($2\pi/3$) about $\mathbf{x} = \mathbf{0}$:

$$R = \begin{pmatrix} -\frac{1}{2} & \frac{\sqrt{3}}{2} \\ \\ -\frac{\sqrt{3}}{2} & -\frac{1}{2} \end{pmatrix}. \tag{2.1}$$

We have also used the the conventions: $\mathcal{P}$ stands for the parity inversion operator, *i.e.*, $\mathcal{P}[f](\mathbf{x}) = f(-\mathbf{x})$; $\mathcal{C}$ stands for the complex conjugate operator, *i.e.*, $\mathcal{C}[f](\mathbf{x}) = \overline{f(\mathbf{x})}$; $\mathcal{R}$ stands for the rotation operator, *i.e.*, $\mathcal{R}[f](\mathbf{x}) = f(R^*\mathbf{x})$.

REMARK 2.1. *Condition 1 is the basic requirement for a loss-free material weight, which ensues that the second order operator associated with the material weight, $\mathcal{L}^A$, is self-adjoint and elliptic. Condition 2 implies that the Bloch theory applies and Conditions 3, 4 imply the commutators between $\mathcal{L}^A$ and the symmetry operators vanish,* i.e., $[\mathcal{PC}, \mathcal{L}^A] = 0$ *and* $[\mathcal{R}, \mathcal{L}^A] = 0$.

Simply speaking, photonic graphene is just an optic media with a hexagonally periodic, $\mathcal{PC}-$ and $\mathcal{R}$-invariant material weight. A honeycomb structured material weight $A(\mathbf{x})$ defined above is generically anisotropic and complex. The full characterization of its Fourier series is given in Section 3.4 of [18]. The simplest nonconstant honeycomb structured media containing the lowest Fourier components is of the form

$$\begin{aligned} A(\mathbf{x}) =& a_0 I + C\ e^{\mathrm{i}\mathbf{k}_1\cdot\mathbf{x}} + RCR^*\ e^{\mathrm{i}\mathbf{k}_2\cdot\mathbf{x}} + R^*CR\ e^{\mathrm{i}(-\mathbf{k}_1-\mathbf{k}_2)\cdot\mathbf{x}} \\ &+ C^T\ e^{-\mathrm{i}\mathbf{k}_1\cdot\mathbf{x}} + RC^TR^*\ e^{-\mathrm{i}\mathbf{k}_2\cdot\mathbf{x}} + R^*C^TR\ \ e^{\mathrm{i}(\mathbf{k}_1+\mathbf{k}_2)\cdot\mathbf{x}}, \end{aligned} \tag{2.2}$$

where C could be any real 2×2 matrix and a_0 is a positive constant ensuring that $A(\mathbf{x})$ is positive definite. If C is symmetric, then $A(\mathbf{x})$ is real. For most natural materials, the material weight is real. However, for meta-materials, the effective material weight can be complex, see for instance [17]. If $C = aI_2$, then $A(\mathbf{x})$ represents an isotropic material.

2.2. Bloch-Floquet theory and Dirac points. For the hexagonal lattice, we define the dual lattice

$$\Lambda_h^* = \mathbb{Z}\mathbf{k}_1 \oplus \mathbb{Z}\mathbf{k}_2,$$

where the dual basis vectors are

$$\mathbf{k}_1 = \frac{4\pi}{\sqrt{3}} \begin{pmatrix} \frac{1}{2} \\ \\ \frac{\sqrt{3}}{2} \end{pmatrix}, \quad \mathbf{k}_2 = \frac{4\pi}{\sqrt{3}} \begin{pmatrix} \frac{1}{2} \\ \\ -\frac{\sqrt{3}}{2} \end{pmatrix}.$$

REMARK 2.2. *The dual lattice Λ_h^* is invariant under the rotation R. To see this, we first define $\mathbf{k}_3 = -\mathbf{k}_1 - \mathbf{k}_2$. Then it is easy to check that $R\mathbf{k}_1 = \mathbf{k}_2$ and $R\mathbf{k}_2 = \mathbf{k}_3$. Consequently, $R\Lambda_h^* = \Lambda_h^*$.*

According to the Bloch-Floquet theory on the elliptic operator with periodic coefficients, the Bloch modes propagating in a perfect photonic graphene satisfy

$$\begin{aligned} &\mathcal{L}^A\Phi(\mathbf{x}) = E\Phi(\mathbf{x}), \\ &\Phi(\mathbf{x}+\mathbf{v}) = e^{\mathrm{i}\mathbf{k}\cdot\mathbf{v}}\Phi(\mathbf{x}), \quad \mathbf{v} \in \Lambda_h \end{aligned} \tag{2.3}$$

Here the quasi-momentum $\mathbf{k}$ takes the value in the Brillouin Zone $\mathbb{B}_h$. For each $\mathbf{k}$, the above eigenvalue problem has discrete spectrum $E_1(\mathbf{k}) \le E_2(\mathbf{k}) \le E_3(\mathbf{k}) \le \cdots$ and the corresponding eigenfunctions, referred to as Bloch modes, are of the form $\Phi_j(\mathbf{x}) = e^{\mathrm{i}\mathbf{k}\cdot\mathbf{x}}\phi_j(\mathbf{x}),\ j = 1, 2, \cdots$ with $\phi_j(\mathbf{x})$ are Λ_h periodic.

Let $\mathbf{K} = \frac{1}{3}(\mathbf{k}_1 - \mathbf{k}_2)$ and $\mathbf{K}' = -\mathbf{K}$. It is shown in [18] that if $A(\mathbf{x})$ is a honeycomb structured material weight, there exists two dispersion bands $E_b(\mathbf{k})$ and $E_{b+1}(\mathbf{k})$ intersect each other at $\mathbf{K}$ and $\mathbf{K}'$ and the dispersion relations are conical nearby. These degenerate points at the dispersion bands, $(E_b(\mathbf{K}_\star), \mathbf{K}_\star)$, $\mathbf{K}_\star = \mathbf{K}, \mathbf{K}'$, are referred to as the Dirac points. Dirac points are unstable under $\mathcal{PC}$-symmetry breaking perturbations. Namely, if $\mathcal{L}^A$ has a Dirac point at $\mathbf{K}_\star$ with the Dirac energy E_D, then $\mathcal{L}^{A+\delta B} \equiv -\nabla \cdot (A(\mathbf{x}) + \delta B(\mathbf{x}))\nabla$ has no Dirac points at $\mathbf{K}_\star$ near the energy E_D provided $B(\mathbf{x})$ is NOT $\mathcal{PC}-$invariant. Specifically, the two intersecting bands at $\mathbf{K}_\star$ separate and a local spectrum gap opens. There are two simple ways to break the $\mathcal{PC}$-symmetry:

(1) $B(\mathbf{x})$ preserves $\mathcal{C}$-symmetry but break the $\mathcal{P}$-symmetry. In other words, $B(\mathbf{x})$ is real and odd. A simple example is

$$B(\mathbf{x}) = [\sin(\mathbf{k}_1 \cdot \mathbf{x}) + \sin(\mathbf{k}_2 \cdot \mathbf{x}) + \sin(\mathbf{k}_3 \cdot \mathbf{x})]I_{2\times 2} \tag{2.4}$$

(2) $B(\mathbf{x})$ preserves $\mathcal{P}$-symmetry but break the $\mathcal{C}$-symmetry. In other words, $B(\mathbf{x})$ is purely imaginary and even. A simple example is

$$B(\mathbf{x}) = [\cos(\mathbf{k}_1 \cdot \mathbf{x}) + \cos(\mathbf{k}_2 \cdot \mathbf{x}) + \cos(\mathbf{k}_3 \cdot \mathbf{x})]\sigma_2 \tag{2.5}$$

where σ_2 is the second Pauli matrix, *i.e.*, $\sigma_2 = \begin{pmatrix} 0 & -\mathrm{i} \\ \mathrm{i} & 0 \end{pmatrix}$ with i as the imaginary unit.

2.3. Domain wall modulated photonic graphene. An interesting phenomenon of the perfect photonic graphene is the conical diffraction, *i.e.*, the wave packets associated with the Dirac points propagate conically in the media [9, 18]. Due to the potential applications, localized and chiral propagations of electromagnetic waves is one of the main research topics related to the so-called topological materials. This can be achieved in the photonic graphene modulated by a domain wall. Specifically, we have the following setup:

1. *Perfect photonic graphene*: Let $A(\mathbf{x})$ be a honeycomb structured material weight. Let $\mathbf{K}_\star = \mathbf{K}$ or $\mathbf{K}'$, and assume that $(\mathbf{K}_\star, E_D)$ is a Dirac point of the operator $\mathcal{L}^A = -\nabla \cdot A\nabla$.
2. *Two perturbed bulk mediums with opposite topological phases*: Let $B(\mathbf{x})$ be a Λ_h-periodic, 2×2 Hermitian matrix such that $\overline{B(-\mathbf{x})} = -B(\mathbf{x})$. The perturbed operator $\mathcal{L}^{A\pm\delta\eta_\infty B} \equiv -\nabla \cdot [A(\mathbf{x}) \pm \delta\eta_\infty B(\mathbf{x})]\nabla$ has no Dirac points near $(\mathbf{K}_\star, E_D)$ and a local spectrum gap opens.
3. *connecting two mediums with a domain wall*: Let $\eta(\zeta)$ is a real bounded function with $\eta(\pm\infty) = \pm\eta_\infty$, for instance, $\eta(\zeta) = \eta_\infty \tanh(\zeta)$. The two perturbed bulk mediums are connected by the domain wall $\eta(\zeta)$ along one direction (referred as the edge), for example, the normal direction of the edge is $\mathbf{k}_2$. In other words, the material weight under consideration becomes $W(\mathbf{x}) = A(\mathbf{x}) + \delta\eta(\delta\mathbf{k}_2 \cdot \mathbf{x})B(\mathbf{x})$.

Our model of a honeycomb structure with an edge is the domain-wall modulated operator:

$$\mathcal{L}^W \equiv -\nabla \cdot [A(\mathbf{x}) + \delta\eta(\delta\mathbf{k}_2 \cdot \mathbf{x})B(\mathbf{x})]\,\nabla. \tag{2.6}$$

The operator $\mathcal{L}^W$ breaks translation invariance with respect to arbitrary elements of the lattice, Λ_h, but is invariant with respect to translation by $\mathbf{v}_1$, parallel to the edge (because $\mathbf{k}_2 \cdot \mathbf{v}_1 = 0$ in (2.6)). Associated with this translation invariance is a parallel quasi-momentum, which we denote by $k_\parallel$. Note that $k_\parallel$ takes that value in $[0, 2\pi]$.

Edge states are solutions of the eigenvalue problem

$$\mathcal{L}^W \Psi(\mathbf{x}; k_\parallel) = E(k_\parallel)\Psi(\mathbf{x}; k_\parallel), \tag{2.7}$$

$$\Psi(\mathbf{x} + \mathbf{v}_1; k_\parallel) = e^{\mathrm{i}k_\parallel}\Psi(\mathbf{x}; k_\parallel), \qquad \text{(propagation parallel to the edge, } \mathbb{R}\mathbf{v}_1\text{)}, \tag{2.8}$$

$$\Psi(\mathbf{x}; k_\parallel) \to 0 \ \text{ as } \ |\mathbf{x} \cdot \mathbf{k}_2| \to \infty, \qquad \text{(localization tranverse to the edge, } \mathbb{R}\mathbf{v}_1\text{)}. \tag{2.9}$$

We refer to a solution pair $(E(k_\parallel), \Psi(\mathbf{x}; k_\parallel))$ of (2.7)–(2.9) as an edge state or edge mode.

In [18], the existence of the edge states at $k_\parallel = \mathbf{K}_\star \cdot \mathbf{v}_1$ in the parameter regime $\delta \ll 1$ is proved and the asymptotic forms of the edge states are given. However, in applications, δ is not small and all edge states (not just near $\mathbf{K}_\star \cdot \mathbf{v}_1$) are useful. Analytical techniques can not achieve this object, and thus numerical methods are required.

3. Gradient recovery method. In this section, we introduce the Bloch-theory based gradient recovery method to solve (2.7)-(2.9).

3.1. Simplified model problem. Let $\Sigma = \mathbb{R}^2/\mathbb{Z}\mathbf{v}_1$ be a cylinder. The fundamental domain for Σ is $\Omega_\Sigma \equiv \{\tau_1\mathbf{v}_1 + \tau_2\mathbf{v}_2 : 0 \le \tau_1 \le 1, \tau_2 \in \mathbb{R}\}$. Let $\Psi(\mathbf{x}; k_\parallel) = e^{\mathrm{i}\frac{k_\parallel}{2\pi}\mathbf{k}_1\cdot\mathbf{x}}p(\mathbf{x}; k_\parallel)$. Then (2.7)–(2.9) is equivalent to the following eigenvalue problem

$$\mathcal{L}^W(k_\parallel)p(\mathbf{x}; k_\parallel) = E(k_\parallel)p(\mathbf{x}; k_\parallel), \tag{3.1}$$

$$p(\mathbf{x} + \mathbf{v}_1; k_\parallel) = p(\mathbf{x}; k_\parallel), \tag{3.2}$$

$$p(\mathbf{x}; k_\parallel) \to 0 \text{ as } |\mathbf{x} \cdot \mathbf{k}_2| \to \infty. \tag{3.3}$$

where

$$\mathcal{L}^W(k_\parallel) = -(\nabla + \mathrm{i}\frac{k_\parallel}{2\pi}\mathbf{k}_1) \cdot W(\nabla + \mathrm{i}\frac{k_\parallel}{2\pi}\mathbf{k}_1). \tag{3.4}$$

It is easy to see that $\mathcal{L}^W(k_\parallel)$ is a self-adjoint operator.

To compute the edge mode, it suffices to consider the spectrum of the operator $\mathcal{L}^W(k_\parallel)$ on the truncated domain

$$\Omega_{\Sigma,L} \equiv \{\tau_1 \mathbf{v}_1 + \tau_2 \mathbf{v}_2 : 0 \le \tau_1 \le 1, -L \le \tau_2 \le L\}. \tag{3.5}$$

Let $W^{k,p}(\Omega_{\Sigma,L})$ be the Sobolev spaces of functions defined on $\Omega_{\Sigma,L}$ with norm $\|\cdot\|_{k,p}$ and seminorm $|\cdot|_{k,p}$. To incorporate the boundary conditions, we define

$$W^{k,p}_{k_\parallel} \equiv \{\Psi : \Psi \in W^{k,p}(\Omega_{\Sigma,L}) \text{ and } \Psi(\mathbf{x}+\mathbf{v}_1) = \Psi(\mathbf{x})\}. \tag{3.6}$$

and

$$W^{k,p}_{k_\parallel,0} \equiv \{\Psi : \Psi \in W^{k,p}_{k_\parallel}(\Omega_{\Sigma,L}) \text{ and } \Psi(\pm L\mathbf{v}_2) = 0\}. \tag{3.7}$$

When $p = 2$, it is simply denoted as $H^1_{k_\parallel}$ or $H^1_{k_\parallel,0}$.

The variation formulation of is (3.1)– (3.3) to find the eigenpair $(E(k_\parallel), \Psi(\mathbf{x}; k_\parallel)) \in \mathbb{R} \times H^1_{k_\parallel,0}$ such that

$$a(p,q) = E(k_\parallel)(p,q), \quad \forall q \in H^1_{k_\parallel,0}, \tag{3.8}$$

where the bilinear form $a(\cdot,\cdot)$ is defined as

$$a(p,q) = \int_{\Omega_{\Sigma,L}} W(\mathbf{x})(\nabla + \mathrm{i}\frac{k_\parallel}{2\pi}\mathbf{k}_1)p(\mathbf{x}) \cdot \overline{(\nabla + \mathrm{i}\frac{k_\parallel}{2\pi}\mathbf{k}_1)q(\mathbf{x})} d\mathbf{x}, \tag{3.9}$$

and the inner product is defined as

$$(p,q) = \int_{\Omega_{\Sigma,L}} p(\mathbf{x})\overline{q(\mathbf{x})} d\mathbf{x}. \tag{3.10}$$

It is easy to see that the bilinear $a(\cdot,\cdot)$ is symmetric and elliptic. According to the spectral theory of linear operator, we know that (3.8) has a countable sequence of real eigenvalues $0 < E_1(k_\parallel) \le E_2(k_\parallel) \le E_3(k_\parallel) \le \cdots \to \infty$ and the corresponding eigenfunctions $p_1(\mathbf{x}; k_\parallel), p_2(\mathbf{x}; k_\parallel), p_3(\mathbf{x}; k_\parallel), \cdots$ are assumed to satisfy

$$a\left(p_i(\mathbf{x}; k_\parallel), p_j(\mathbf{x}; k_\parallel)\right) = E_i(k_\parallel)\left(p_i(\mathbf{x}; k_\parallel), p_j(\mathbf{x}; k_\parallel)\right) = \delta_{ij}.$$

3.2. Finite element approximation. To simplify the imposing of the periodic boundary, we shall consider the uniform triangulation of $\Omega_{\Sigma,L}$. To generate a uniform triangulation $\mathcal{T}_h$ with mesh size $h = \frac{\|\mathfrak{v}_1\|}{N}$ of $\Omega_{\Sigma,L}$, we firstly divide $\Omega_{\Sigma,L}$ into $2LN^2$ sub-rhombuses with mesh size $h = \frac{\|\mathfrak{v}_1\|}{N}$ and divide each sub-rhombus into two triangles. We define the standard linear finite element space with periodic boundary condition in $\mathfrak{v}_1$ as

$$V_h = \{v \in C(\Omega_{\Sigma,L}) : q|_T \in \mathbb{P}_1(T), \forall T \in \mathcal{T}_h \text{ and } q(\mathbf{x}+\mathbf{v}_1) = q(\mathbf{x})\}. \tag{3.11}$$

with $\mathbb{P}_k$ being the space consisting of polynomials of degree up to k and the corresponding finite element space with homogeneous boundary condition in $\mathfrak{v}_2$ as

$$V_{h,0} = V_h \cap H^1_{k_\parallel,0}. \tag{3.12}$$

The finite element discretization of the eigenvalue problem (3.8) is to find the eigenpair $(E_h(k_\parallel), p_h(\mathbf{x}; k_\parallel)) \in \mathbb{R} \times V_{h,0}$ such that

$$a(p_h, q_h) = E_h(k_\parallel)(p_h, q_h), \quad \forall q_h \in V_{h,0}. \tag{3.13}$$

Similar as (3.8), (3.13) has a finite sequence of eigenvalues $0 < E_{1,h}(k_\parallel) \leq E_{2,h}(k_\parallel) \leq \cdots \leq E_{n_h,h}(k_\parallel)$ and the corresponding eigenfunctions are assumed to satisfy

$$a\left(p_{i,h}(\mathbf{x}; k_\parallel), p_{j,h}(\mathbf{x}; k_\parallel)\right) = E_i(k_\parallel)\left(p_{i,h}(\mathbf{x}; k_\parallel)\right., p_{j,h}(\mathbf{x}; k_\parallel)) = \delta_{ij}.$$

For the finite element approximation, the following error estimates is well established in [4, 29]

THEOREM 3.1. *Suppose $p_i(\mathbf{x}; k_\parallel) \in H^2_{k_\parallel}$. Then we have*

$$E_i(k_\parallel) \leq E_{i,h}(k_\parallel) \leq E_i(k_\parallel) + Ch^2; \tag{3.14}$$

$$\|p_i - p_{i,h}\|_1 \leq Ch; \tag{3.15}$$

$$\|p_i - p_{i,h}\|_0 \leq Ch^2. \tag{3.16}$$

The following property of the eigenvalue and eigenfunction approximation will be used in the analysis

LEMMA 3.2. *Let $(E(k_\parallel), p(\mathbf{x}; k_\parallel))$ be the solution of of the eigenvalue problem (3.8). Then for any $q \in H^1_{k_\parallel,0}$, we have*

$$\frac{a(p,q)}{\|q\|_0^2} - E(k_\parallel) = \frac{a(p-q, p-q)}{\|q\|_0^2} - E(k_\parallel)\frac{\|p-q\|_0^2}{\|q\|_0^2} \tag{3.17}$$

3.3. Superconvergent post-processing. To identify edge modes, we need to compute a series of eigenvalue problems with higher accuracy for $k_\parallel \in [0, 2\pi]$. To achieve higher accuracy, we can use higher-order elements. But it will involve higher computational complexity. To avoid the computational complexity, we use the linear element and then adopt a recovery procedure to increase the eigenpair approximation accuracy [25].

Let $G_h : V_h \to V_h \times V_h$ denote the polynomial preserving recovery operator introduced in [24, 33]. For any function $q_h \in V_h$, $G_h q_h$ is a function in $V_h \times V_h$. To define $G_h v_h$, it suffices to define the value of $G_h q_h$ at every nodal point. Let $\mathcal{N}_h$ denote the set of all nodal points of $\mathcal{T}_h$. Note that $\mathcal{N}_h$ is the set of all vertices of $\mathcal{T}_h$. For any $z \in \mathcal{N}_h$, construct a local patch of the element $\mathcal{K}_z$ which contains at least six nodal points. The key idea of PPR is to fit a quadratic polynomial $p_z \in \mathcal{P}_z(\mathcal{K}_z)$ in the following least-squares sense

$$p_z = \arg \min_{p \in \mathbb{P}_2(\mathcal{K}_z)} \sum_{\tilde{z} \in \mathcal{N}_h \cap \mathcal{K}_z} (q_h - p)^2(\tilde{z}) \tag{3.18}$$

Then the recovered gradient at z is defined as

$$(G_h q_h)(z) = \nabla p_z(z). \tag{3.19}$$

The global recovered gradient is $G_h q_h = (G_h q_h)(z)\phi_z(\mathbf{x})$ where $\{\phi_z\}$ is set of nodal basis of V_h.

To improve the accuracy of eigenvalue approximation, we set $q = p_h$ in (3.17) which implies

$$E_h(k_\parallel) - E(k_\parallel) = a(p - p_h, p - p_h) - E(k_\parallel)\|p - p_h\|_0^2 \tag{3.20}$$

It is obvious that the first term dominates in the eigenvalue approximation error. The idea of [25] for Laplace eigenvalue problem is to subtract a good approximation of the first term from both sides by replacing the exact gradient by recovered gradient. In our case, it is much more complicated since the energy error contains both ∇p and p. Our idea is to only consider the leading part in the energy error . Thus, we define the recovered eigenvalue as follows

$$\widehat{E_h}(k_\parallel) = E_h(k_\parallel) - \|W^{1/2}(\nabla p_h - G_h p_h)\|_0. \tag{3.21}$$

To show the superconvergence of the recovered eigenvalue, the following supercloseness result is needed which can be found in [19]

LEMMA 3.3. *Let $I_h p$ be the interpolation of p into the finite element space V_h. If $p \in H^3_{k_\parallel}$, then we have*

$$a(p - I_h p, q_h) \le Ch^2\|p\|_3\|q_h\|_1, \quad \forall q_h \in V_{h,0}. \tag{3.22}$$

Proof. We can prove the lemma use the similar idea in [19]. □

Based on the above lemma, we can show the superconvergence of recovered gradient as following:

THEOREM 3.4. *Let G_h be the polynomial preserving recovery operator defined in the above. Then for any eigenfunction $p_{i,h}$ corresponding to the eigenvalue $E_{i,h}(k_\parallel)$, there exists an eigenfunction p_i corresponding to $E_i(k_\parallel)$ such that*

$$\|W^{1/2}(\nabla p_i - G_h p_{i,h})\|_0 \le Ch^2\|p_i\|_3. \tag{3.23}$$

Proof. By (3.8) and (3.13), we have

$$\begin{aligned} &a(p_{i,h} - p_i, q_h) \\ =&E_{i,h}(k_\parallel)(p_{i,h}, q_h) - E_i(k_\parallel)(p_i, q_h) \\ =&E_{i,h}(k_\parallel)(p_{i,h} - p_i, q_h) + (E_{i,h}(k_\parallel) - E_i(k_\parallel))(p_i, q_h). \end{aligned} \tag{3.24}$$

It implies that

$$\begin{aligned} &a(p_{i,h} - I_h p_i, q_h) \\ =&a(p_i - I_h p_i, q_h) + E_{i,h}(k_\parallel)(p_{i,h}, q_h) - E_i(k_\parallel)(p_i, q_h) \\ =&a(p_i - I_h p_i, q_h) + E_{i,h}(k_\parallel)(p_{i,h} - p_i, q_h) + (E_{i,h}(k_\parallel) - E_i(k_\parallel))(p_i, q_h) \\ \le&Ch^2\|p_i\|_3\|q_h\|_1; \end{aligned} \tag{3.25}$$

where we have used the Theorem 3.1 and Lemma 3.3. Taking $q_h = p_{i,h} - I_h p_i$ implies that

$$\|p_{i,h} - I_h p_i\|_1 \le Ch^2\|p_i\|_3 \tag{3.26}$$

Thus, we have

$$\begin{aligned}
&\|W^{1/2}(\nabla p_i - G_h p_{i,h})\|_0 \\
\leq&\|W^{1/2}(\nabla p_i - G_h I_h p_i)\|_0 + \|W^{1/2}(G_h I_h p_i - G_h p_{i,h})\|_0 \\
\leq&\|(\nabla p_i - G_h I_h p_i)\|_0 + \|(G_h I_h p_i - G_h p_{i,h})\|_0 \\
\leq&\|(\nabla p_i - G_h I_h p_i)\|_0 + \|\nabla(I_h p_i - p_{i,h})\|_0 \\
\leq&Ch^2\|p_i\|_3.
\end{aligned} \tag{3.27}$$

where we have use Lemma 4.3 in [13] and (3.26). □

Using the above theorem, we can prove the following superconvergence result for recovered eigenvalues

THEOREM 3.5. *Let $E_{i,h}(k_\parallel)$ be the approximate eigenvalue of $E_i(k_\parallel)$. Then we have*

$$|\widehat{E}_{i,h}(k_\parallel) - E_i(k_\parallel)| \leq Ch^3\|p_i\|_3^2. \tag{3.28}$$

Proof. By the Lemma 3.2 and (3.21), we have

$$\begin{aligned}
&\widehat{E}_{i,h}(k_\parallel) - E_i(k_\parallel) \\
=&a(p_i - p_{i,h}, p_h - p_{i,h}) - \|W^{1/2}(\nabla p_h - G_h p_h)\|_0^2 - E_i(k_\parallel)\|p_i - p_{i,h}\|_0^2 \\
=&(W(\nabla + \frac{\mathrm{i}k_\parallel}{2\pi}\mathbf{k}_1)(p_i - p_{i,h}), (\nabla + \frac{\mathrm{i}k_\parallel}{2\pi}\mathbf{k}_1)(p_i - p_{i,h})) - \\
&\|W^{1/2}(\nabla p_h - G_h p_h)\|_0^2 - E_i(k_\parallel)\|p_i - p_{i,h}\|_0^2 \\
=&(W(\nabla p_i - G_h p_{i,h}), \nabla p_i - G_h p_{i,h}) - \frac{\mathrm{i}k_\parallel}{2\pi}(W\nabla(p_i - p_{i,h}), \mathbf{k}_1(p_i - p_{i,h})) + \\
&\frac{\mathrm{i}k_\parallel}{2\pi}(\mathbf{k}_1(p_i - p_{i,h}), W\nabla(p_i - p_{i,h})) + \frac{k_\parallel^2}{4\pi^2}(W\mathbf{k}_1(p_i - p_{i,h}), \mathbf{k}_1(p_i - p_{i,h})) + \\
&\|W^{1/2}(\nabla p_h - G_h p_h)\|_0^2 - E_i(k_\parallel)\|p_i - p_{i,h}\|_0^2 \\
=&(W(\nabla p_i - G_h p_{i,h}), \nabla p_i - G_h p_{i,h}) - \frac{\mathrm{i}k_\parallel}{2\pi}(W\nabla(p_i - p_{i,h}), \mathbf{k}_1(p_i - p_{i,h})) + \\
&\frac{\mathrm{i}k_\parallel}{2\pi}(\mathbf{k}_1(p_i - p_{i,h}), W\nabla(p_i - p_{i,h})) + \frac{k_\parallel^2}{4\pi^2}(W\mathbf{k}_1(p_i - p_{i,h}), \mathbf{k}_1(p_i - p_{i,h})) + \\
&2\,\mathrm{Re}\,(W(\nabla p_i - G_h p_{i,h}), G_h p_{i,h} - \nabla p_{i,h}) - E_i(k_\parallel)\|p_i - p_{i,h}\|_0^2 \\
\leq&C\big(\|\nabla p_i - G_h p_{i,h}\|_0^2 + \|p_i - p_{i,h}\|_0\|\nabla(p_i - p_{i,h})\|_0 \\
&\quad\|p_i - p_{i,h}\|_0^2 + \|\nabla p_i - G_h p_{i,h}\|_0^2\|\nabla p_{i,h} - G_h p_{i,h}\|_0^2 + \|p_i - p_{i,h}\|_0^2)\big) \\
\leq&Ch^3\|p_i\|_3^2.
\end{aligned}$$

□

REMARK 3.1. *We should point out that the error bound in* (3.28) *is not sharp. Our numerical results indicate that the real error bound should be $\mathcal{O}(h^4)$.*

3.4. Efficient Implementation. In this section, we present an efficient implementation of the proposed method. One of our key observation is that the gradient recovery procedure is just two multiplications of a sparse matrix and a vector, which can be done within $\mathcal{O}(N)$ operations. For a sake of clarity, we rewrite G_h as

$$G_h p = \begin{pmatrix} G_h^x p \\ G_h^y p \end{pmatrix}. \tag{3.29}$$

Notice that gradient recovery operator G_h is a linear bounded operator from V_h to $V_h \times V_h$. In other words, G_h^x and G_h^y are both linear bounded operators from V_h to V_h. It is well known that every linear operator (linear transform) from one finite dimension vector space to itself can be rephrase a matrix linear transform [3]. Suppose $\{\phi_i\}_{i=1}^N$ is the standard nodal basis function for V_h. Let $\mathbf{b}$ be the vector of basis functions, i.e. $\mathbf{b} = (\phi_1, \cdots, \phi_N)^T$. Then for every function $v_h \in V_h$, it can be rewritten in the following form

$$v_h = \sum_1^N v_i \phi_i = \mathbf{v}^T \mathbf{b}, \tag{3.30}$$

where $\mathbf{v} = (v_1, \cdots, v_N)^T$ and v_i is the value of v_h at nodal point z_i. Similarly, the recovered gradient $G_h v_h$ can also be rephrase as

$$G_h v_h = [G_h^x v_h, G_h^y v_h] = [\mathbf{v_x}^T \mathbf{b}, \mathbf{v_y}^T \mathbf{b}] \tag{3.31}$$

where $\mathbf{v_x}$ and $\mathbf{v_y}$ are the vectors of recovered gradient at nodal points. Since G_h^x and G_h^y are two linear bounded operator V_h to V_h, there exist two matrices $\mathbf{G_h^x} \in \mathbb{R}^{N\times N}$ and $\mathbf{G_h^y} \in \mathbb{R}^{N\times N}$ such that

$$\mathbf{v_x} = \mathbf{G_h^x v} \text{ and } \mathbf{v_y} = \mathbf{G_h^y v}. \tag{3.32}$$

Here $\mathbf{G_h^x}$ and $\mathbf{G_h^y}$ are called the first order differential matrices. From the definition of polynomial preserving recovery, it is obvious $\mathbf{G_h^x}$ and $\mathbf{G_h^y}$ are both sparse matrices.

To efficiently implement the algorithm, we rewrite the bilinear form $a(\cdot,\cdot)$ as

$$\begin{aligned} a(p,q) &= \int_{\Omega_{\Sigma,L}} W(\mathbf{x})(\nabla + \mathrm{i}\frac{k_\parallel}{2\pi}\mathbf{k}_1)p(\mathbf{x}) \cdot \overline{(\nabla + \mathrm{i}\frac{k_\parallel}{2\pi}\mathbf{k}_1)q(\mathbf{x})} d\mathbf{x} \\ &= \int_{\Omega_{\Sigma,L}} W(\mathbf{x})\nabla p(\mathbf{x}) \cdot \overline{\nabla q(\mathbf{x})} d\mathbf{x} - \\ &\quad \mathrm{i}\frac{k_\parallel}{2\pi} \int_{\Omega_{\Sigma,L}} W(\mathbf{x})\nabla p(\mathbf{x}) \cdot \overline{\mathbf{k}_1 q(\mathbf{x})} d\mathbf{x} + \\ &\quad \mathrm{i}\frac{k_\parallel}{2\pi} \int_{\Omega_{\Sigma,L}} W(\mathbf{x})\mathbf{k}_1 q(\mathbf{x}) \cdot \overline{\nabla p(\mathbf{x})} d\mathbf{x} + \\ &\quad \frac{k_\parallel^2}{4\pi^2} \int_{\Omega_{\Sigma,L}} W(\mathbf{x})\mathbf{k}_1 q(\mathbf{x}) \cdot \overline{\mathbf{k}_1 q(\mathbf{x})} d\mathbf{x}. \end{aligned} \tag{3.33}$$

Let $\mathbf{A}$, $\mathbf{B}$, and $\mathbf{C}$ be the sparse matrices of the bilinear form $\int_{\Omega_{\Sigma,L}} W(\mathbf{x})\nabla p(\mathbf{x}) \cdot \overline{\nabla q(\mathbf{x})} d\mathbf{x}$, $\int_{\Omega_{\Sigma,L}} W(\mathbf{x})\nabla p(\mathbf{x}) \cdot \overline{\mathbf{k}_1 q(\mathbf{x})} d\mathbf{x}$, and $\int_{\Omega_{\Sigma,L}} W(\mathbf{x})\mathbf{k}_1 p(\mathbf{x}) \cdot \overline{\mathbf{k}_1 q(\mathbf{x})} d\mathbf{x}$, respectively. Then the total sparse matrix can be represented as

$$\mathbf{S} = \mathbf{A} - \mathrm{i}\frac{k_\parallel}{2\pi}\mathbf{B} + \mathrm{i}\frac{k_\parallel}{2\pi}\mathbf{B}^T + \frac{k_\parallel^2}{4\pi^2}\mathbf{C}. \tag{3.34}$$

In addition, we use $\mathbf{M}$ to denote the mass matrix.

The above algorithm can be summarized in Algorithm 1.

Algorithm 1: Superconvergent post-processing algorithm for computing edge mode

Generate a uniform mesh $\mathcal{T}_h$;
Construct sparse matrices $\mathbf{A}$, $\mathbf{B}$, $\mathbf{C}$, $\mathbf{M}$, $\mathbf{G_x}$, and $\mathbf{G_y}$;
Let $k = linspace(0, 2\pi, K)$;
for j = *1:K* **do**
    Let $k_\parallel = k(j)$.;
    Form the big stiffness matrix $\mathbf{S} = \mathbf{A} - \mathrm{i}\frac{k_\parallel}{2\pi}\mathbf{B} + \mathrm{i}\frac{k_\parallel}{2\pi}\mathbf{B}^T + \frac{k_\parallel^2}{4\pi^2}\mathbf{C}$;
    Solve the generalized eigenvalue problem $\mathbf{Sv} = E_h(k_\parallel)\mathbf{Mv}$;
    Compute the recovered gradient by doing two sparse matrix-vector multiplications $\mathbf{v_x} = \mathbf{G_h^x v}$ and $\mathbf{v_y} = \mathbf{G_h^y v}$;
    Update the eigenvalue

$$\widehat{E_h}(k_\parallel) = E_h(k_\parallel) - \|W^{1/2}(\nabla p_h - G_h p_h)\|^2_{0,\Omega_{\Sigma,L}}.$$

end

From Algorithm 1, the cost of gradient recovery is about $\mathcal{O}(N)$ and the most expansive part is computational of the generalized eigenvalue.

4. Numerical Examples. In this section, we present several numerical examples to show the efficiency of the proposed Bloch theory-based gradient recovery method. Our method and analysis apply for any honeycomb structured media with a domain wall modulation given in Section 2. The material weight is always of the form

$$W(\mathbf{x}) = A(\mathbf{x}) + \delta\eta(\delta\mathbf{k}_2 \cdot \mathbf{x})B(\mathbf{x}). \tag{4.1}$$

In the numerical examples, $A(\mathbf{x})$ is given in (2.2), $B(\mathbf{x})$ is given in (2.4) or (2.5) and $\eta(\zeta) = \tanh(\zeta)$. These simple choices of material weights are sufficient enough to demonstrate our method and analysis. The first example is to numerically verify the superconvergence of the method, and the other examples are devoted to the computation of edge modes for the $\mathcal{P}$-symmetry and $\mathcal{C}$-symmetry breaking cases in honeycomb structures.

4.1. Verification of superconvergence. In this example, we present a comparison of eigenvalues in (2.7)-(2.9) computed by the standard finite element method and gradient recovery method, respectively. In this test, we take $N = 20$, 40, 80, 160, 320, 640 and $L = 10$. $A(\mathbf{x})$ is given in (2.2) with $a_0 = 23$, $C = \begin{pmatrix} -\frac{1}{2} & 0 \\ 0 & -\frac{1}{2} \end{pmatrix}$. $B(\mathbf{x})$ is given in (2.4). $\delta = 2$. Namely,

$$A(\mathbf{x}) = \left[23 - \cos(\mathbf{x}\cdot\mathbf{k}_1) - \cos(\mathbf{x}\cdot\mathbf{k}_2) - \cos(\mathbf{x}\cdot\mathbf{k}_3)\right] I_{2\times 2}, \tag{4.2}$$

$$B(\mathbf{x}) = \left[\sin(\mathbf{x}\cdot\mathbf{k}_1) + \sin(\mathbf{x}\cdot\mathbf{k}_2) + \sin(\mathbf{x}\cdot\mathbf{k}_3)\right] I_{2\times 2}. \tag{4.3}$$

We define the two following errors

$$Err_i = \frac{|E_{i,h_j} - E_{i,h_{j+1}}|}{E_{i,h_{j+1}}},$$

and

$$\widehat{Err}_i = \frac{|\widehat{E}_{i,h_j} - \widehat{E}_{i,h_{j+1}}|}{\widehat{E}_{i,h_{j+1}}}.$$

In this test, we take $\mathbf{k} = 0.28\mathbf{k}_1$ and focus on the computation of the first six eigenvalues. In Figure 4.1, we plot the convergence rates for the relative error of eigenvalues computed by the standard finite element method. It indicates that the convergence rate is $\mathcal{O}(h^2)$, which is consistent with the theoretical result in Theorem 3.1. In Figure 4.2, we plot the convergence rates for the relative error of the eigenvalues computed by the Bloch theory-based gradient recovery method. It converges at the superconvergent rate of $\mathcal{O}(h^4)$. As explained in Remark 3.1, it is better than results predicted by Theorem 3.5. The comparison shows that the gradient recovery method outperforms the standard finite element method in the several digits magnitude. In the following examples, we shall only show the eigenvalues computed by the gradient recovery method.

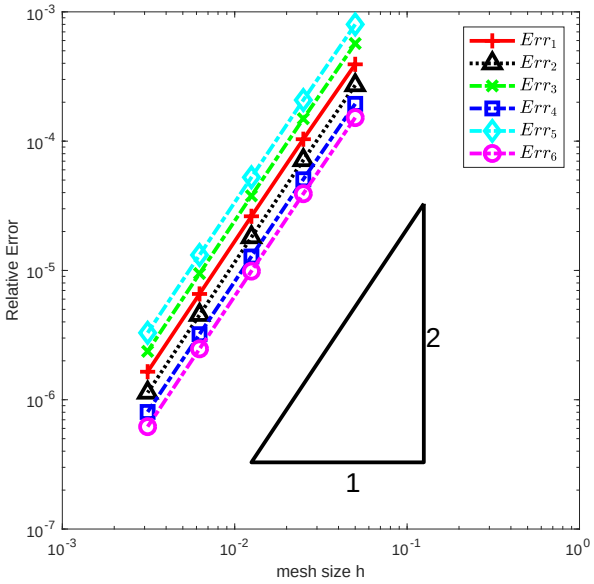

Fig. 4.1: Convergence rates of the eigenvalues for the case (4.2)-(4.3) computed by the standard finite element method.

4.2. Computational of edge modes for $\mathcal{P}$-symmetry breaking. Here we test the $\mathcal{P}$-symmetry breaking case, *i.e.,* $B(\mathbf{x})$ is given in (2.4). In all the following tests, we take the $N = 64$ and the mesh size is $h = \frac{1}{64}$.

Test Case 1: In this test, we consider the case that

$$A(\mathbf{x}) = [23 - \cos(\mathbf{x}\cdot\mathbf{k}_1) - \cos(\mathbf{x}\cdot\mathbf{k}_2) - \cos(\mathbf{x}\cdot\mathbf{k}_3)]\, I_{2\times 2}, \tag{4.4}$$

$$B(\mathbf{x}) = [\sin(\mathbf{x}\cdot\mathbf{k}_1) + \sin(\mathbf{x}\cdot\mathbf{k}_2) + \sin(\mathbf{x}\cdot\mathbf{k}_3)]\, I_{2\times 2}, \tag{4.5}$$

with the parameter $\delta = 6$.

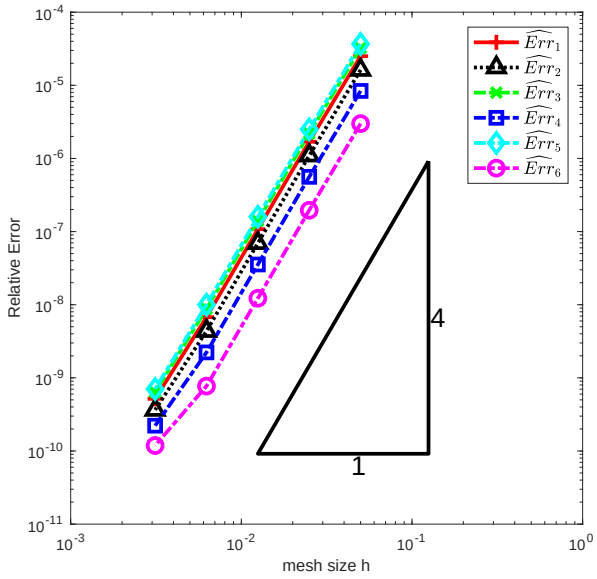

Fig. 4.2: Convergence rates of the eigenvalues for the case (4.2)-(4.3) computed by the Bloch-theory based gradient recovery method.

We firstly run our test with $L = 10$. We graph the first twenty-five eigenvalues for $k_{\|} \in [0, 2\pi]$ in Figure 4.3, from which one can see that the red line corresponding to the 20^{th} eigenvalue is isolated from other lines. Based on the analysis in [18], this curve corresponds to the edge mode, and all other eigenvalues belong to the continuous spectrum. In Figure 4.4, we show the contour graph of the modulus of the 19^{th}, 20^{th}, and 21^{th} eigenvalues when $k_{\|} = \frac{2\pi}{3}$. In this graph and all the other contour graphs in this paper , we select $\mathbf{v}_2$ as x-axis and $\mathbf{v}_1$ as y-axis. From Figure 4.4b, we clearly obverse the 20^{th} eigenfunction (edge mode) is periodic in $\mathbf{v}_1$ and localized at the center along $\mathbf{v}_2$.

To make a comparison, we repeat our test for $L = 15$. In Figure 4.5, we show the plot of the first thirty-five recovered eigenvalues. The edge mode is corresponding to the 30^{th} eigenvalue. From Figure 4.6b, we see more clearly that the eigenvalue is localized at the center along $\mathbf{v}_2$.

Test Case 2: In this test, we consider the case that

$$A(\mathbf{x}) = [4 - \cos(\mathbf{x} \cdot \mathbf{k}_1) - \cos(\mathbf{x} \cdot \mathbf{k}_2) - \cos(\mathbf{x} \cdot \mathbf{k}_3)]\, I_{2\times 2}, \tag{4.6}$$

$$B(\mathbf{x}) = [\sin(\mathbf{x} \cdot \mathbf{k}_1) + \sin(\mathbf{x} \cdot \mathbf{k}_2) + \sin(\mathbf{x} \cdot \mathbf{k}_3)]\, I_{2\times 2}, \tag{4.7}$$

with the parameter $\delta = 1$.

We compute the edge mode with $L = 10$. The first twenty-five eigenvalues are shown in Figure 4.7. Similarly, we find that the 20^{th} eigenvalue is isolated from other eigenvalues, which is marked by 'X' and plotted in red. In Figure 4.8, we show the contour of the module of the some eigenfunctions with $k_{\|} = \frac{2\pi}{3}$, which confirms that the 20^{th} eigenvalue is the edge mode.

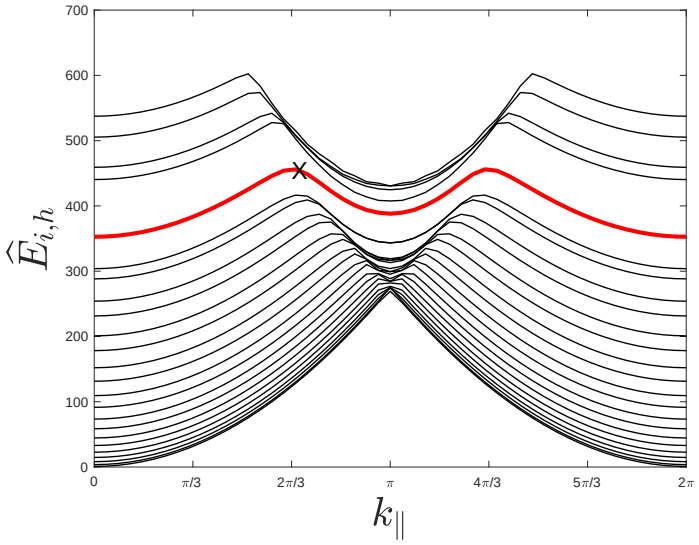

Fig. 4.3: Eigenvalues computed by gradient recovery methods for the $\mathcal{P}$-symmetry breaking case (4.4)-(4.5) with $L = 10$. The edge mode is corresponding to the line marked by 'X'.

4.3. Computation of edge modes for $\mathcal{C}$-symmetry breaking. We consider the $\mathcal{C}$-symmetry breaking case. Specifically,

$$A(\mathbf{x}) = [4 - \cos(\mathbf{x}\cdot\mathbf{k}_1) - \cos(\mathbf{x}\cdot\mathbf{k}_2) - \cos(\mathbf{x}\cdot\mathbf{k}_3)]I_{2\times 2}, \tag{4.8}$$

$$B(\mathbf{x}) = [\cos(\mathbf{x}\cdot\mathbf{k}_1) + \cos(\mathbf{x}\cdot\mathbf{k}_2) + \cos(\mathbf{x}\cdot\mathbf{k}_3)]\sigma_2, \tag{4.9}$$

and the parameter $\delta = 1$. In Figure 4.9, we plot the first twenty-five eigenvalues $\widehat{E}_{i,h}$ in terms of $k_{\|}$. At the point $k_{\|} = \frac{2\pi}{3}$, we observe that the 19^{th}, 20^{th}, and 21^{th} eigenvalues are isolated from other eigenvalues. It looks like there are three edge modes. To investigate the situation, we graph the contour of the module of the those eigenfunctions in Figure 4.10. From Figure 4.10, the 19^{th} and 20^{th} eigenfunctions are localized at the boundary but the 21^{th} eigenfunction is localized at the center. Based on the analysis in [18], the 19^{th} and 20^{th} eigenfunctions are the pseudo edge modes and the only edge mode is the 21th eigenfunction.

4.4. Computation of the edge mode in the anisotropic case with $\mathcal{C}$-symmetry breaking. In this subsection, we consider the numerical results with anisotropic coefficients. Specifically, $A(\mathbf{x})$ is given in (2.2) with

$$a_0 = 10, \quad C = \begin{pmatrix} -1 & 2 \\ 0 & -2 \end{pmatrix}, \tag{4.10}$$

$$B(\mathbf{x}) = [\cos(\mathbf{x}\cdot\mathbf{k}_1) + \cos(\mathbf{x}\cdot\mathbf{k}_2) + \cos(\mathbf{x}\cdot\mathbf{k}_3)]\sigma_2 \tag{4.11}$$

and the parameter $\delta = 1$. In Figure 4.11, we plot the first twenty-five eigenvalues $\widehat{E}_{i,h}$ in terms of $k_{\|}$. Similar to the numerical results in previous section, we observe that 19^{th}, 20^{th}, and 21^{th} eigenvalues are isolated from other eigenvalues at $k_{\|} = \frac{2\pi}{3}$.

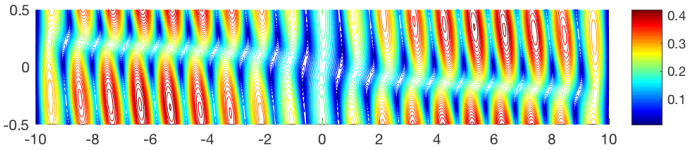

(a) The 19th eigenfunction

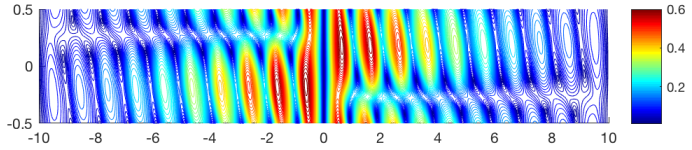

(b) The 20th eigenfunction

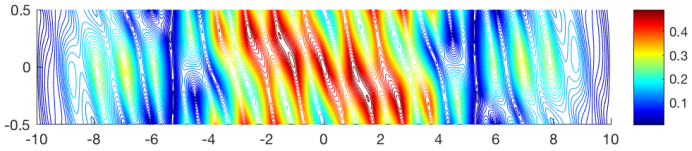

(c) The 21th eigenfunction

Fig. 4.4: Contour of the module of the eigenfunctions computed by gradient recovery method with $L = 10$ for the $\mathcal{P}$-symmetry breaking case (4.4)-(4.5) when $k_{\|} = \frac{2\pi}{3}$. We choose $\mathbf{v}_2$ as x-axis and $\mathbf{v}_1$ as y-axis. The 20th eigenfunction is the edge mode, which is periodic in $\mathbf{v}_1$ and localized at the center along $\mathbf{v}_2$.

The red curve is the curve corresponding to the 21^{th} eigenvalue. In Figures 4.12, we draw the contour plot of the corresponding eigenfunctions when $k_{\|} = \frac{2\pi}{3}$. We can see that the eigenfunctions corresponding to the 19^{th} and 20^{th} eigenvalues are localized at the boundary, while the eigenfunction corresponding to the 21^{th} eigenvalue is localized at the center which is the edge mode.

5. Conclusion. Photonic graphene is an “artificial graphene" which admints subtle propagating modes of electromagnetic waves. It is also an important topological material which support topological edge states. These states propagates along the edge without any back scattering when passing through a defect. So they have wide applications in many optical systems. Unfortunately, only few analytical results which work in a very narrow parameter regime have been given, see for example [18]. How to numerically compute these modes and associated gradients accurately to construct the whole electromagnetic fields under propagation is a very important question in applications. To solve this problem, we propose a novel superconvergent finite element method based on Bloch theory and gradient recovery techniques for the computation of such states in photonic graphene with a domain wall modulation. We analyze the accuracy of this method and show its efficiency by computing the $\mathcal{P}$-symmetry and $\mathcal{C}$-symmetry breaking cases in honeycomb structures. Our numerical results are consistent with the analysis in [18]. At present, this work only focuses on the static modes. In the future, we shall study the dynamics of such modes. This requires us to

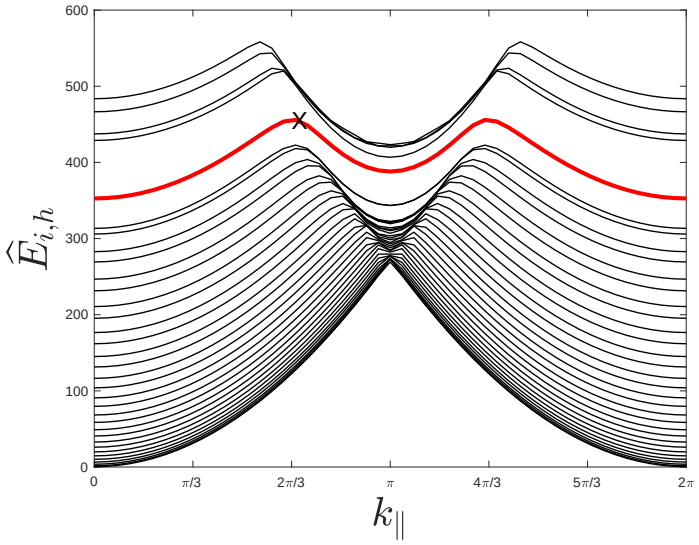

Fig. 4.5: Eigenvalues computed by gradient recovery methods for the $\mathcal{P}$-symmetry breaking case (4.4)-(4.5) with $L = 15$. The edge mode is corresponding to the line marked by 'X'.

(1) recover the full electromagnetic fields from these modes computed by the super-convergent finite element method; (2) compute the time evolution equation (Maxwell equation). How to utilize the high accurate edge states to perform their dynamics will be further investigated.

REFERENCES

[1] M J Ablowitz, S D Nixon, and Y Zhu, *Conical diffraction in honeycomb lattices*, Physical Review A, 79 (2009), p. 053830.

[2] M. Ainsworth and J. T. Oden, *A posteriori error estimation in finite element analysis*, Pure and Applied Mathematics (New York), Wiley-Interscience [John Wiley & Sons], New York, 2000.

[3] S. Axler, *Linear algebra done right*, Undergraduate Texts in Mathematics, Springer, Cham, third ed., 2015.

[4] I. Babuška and T. Strouboulis, *The finite element method and its reliability*, Numerical Mathematics and Scientific Computation, The Clarendon Press, Oxford University Press, New York, 2001.

[5] I. Babušska, T. Strouboulis, C. S. Upadhyay, S. K. Gangaraj, and K. Copps, *Validation of a posteriori error estimators by numerical approach*, Internat. J. Numer. Methods Engrg., 37 (1994), pp. 1073–1123.

[6] A. Bensoussan, J. L. Lions, and G. Papanicolaou, *Asymptotic analysis for periodic structures*, vol. 5 of Studies in Mathematics and its Applications, North-Holland, Amsterdam-New York, 1978.

[7] C. Carstensen and S. Bartels, *Each averaging technique yields reliable a posteriori error control in FEM on unstructured grids. I. Low order conforming, nonconforming, and mixed FEM*, Math. Comp., 71 (2002), pp. 945–969.

[8] H. Chen, H. Guo, Z. Zhang, and Q. Zou, *A C^0 linear finite element method for two fourth-order eigenvalue problems*, IMA J. Numer. Anal., 37 (2017), pp. 2120–2138.

[9] C L Fefferman and M I Weinstein, *Wave packets in honeycomb structures and two-dimensional dirac equations*, Comm. Math. Phys., 2.

[10] L. Formaggia and S. Perotto, *New anisotropic a priori error estimates*, Numer. Math., 89

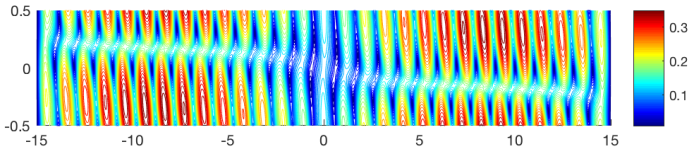

(a) The 29th eigenfunction

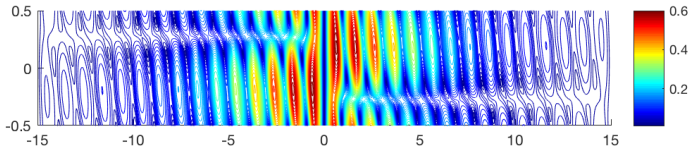

(b) The 30th eigenfunction

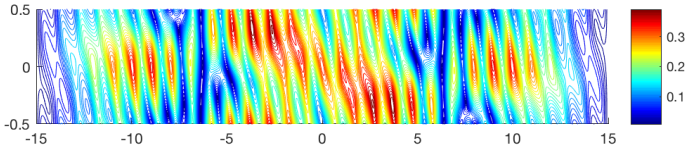

(c) The 31th eigenfunction

Fig. 4.6: Contour of the module of the eigenfunctions computed by gradient recovery method with $L = 15$ for the $\mathcal{P}$-symmetry breaking case (4.4)-(4.5) when $k_{\|} = \frac{2\pi}{3}$. We choose $\mathbf{v}_2$ as x-axis and $\mathbf{v}_1$ as y-axis. The 30th eigenfunction is the edge mode, which is periodic in $\mathbf{v}_1$ and localized at the center along $\mathbf{v}_2$.

(2001), pp. 641–667.

[11] ———, *Anisotropic error estimates for elliptic problems*, Numer. Math., 94 (2003), pp. 67–92.

[12] A. K. Geim and K. S. Novoselov, *The rise of graphene*, Nature materials, 6 (2007), pp. 183–191.

[13] H. Guo and X. Yang, *Polynomial preserving recovery for high frequency wave propagation*, J. Sci. Comput., 71 (2017), pp. 594–614.

[14] H. Guo, Z. Zhang, and R. Zhao, *Superconvergent two-grid methods for elliptic eigenvalue problems*, J. Sci. Comput., 70 (2017), pp. 125–148.

[15] H. Guo, Z. Zhang, and Q. Zou, *A C^0 linear finite element method for biharmonic problems*, J. Sci. Comput., (2017).

[16] W. Huang and R. D. Russell, *Adaptive moving mesh methods*, vol. 174 of Applied Mathematical Sciences, Springer, New York, 2011.

[17] A. B. Khanikaev, S. H. Mousavi, W.-K. Tse, M. Kargarian, A. H. MacDonald, and G. Shvets, *Photonic topological insulators*, Nature materials, 12 (2013), pp. 233–239.

[18] J. P. Lee-Thorp, M. I. Weinstein, and Y. Zhu, *Elliptic operators with honeycomb symmetry: Dirac points, edge states and applications to photonic graphene*, arXiv:1710.03389, (2017).

[19] Q. Lin and J. Xu, *Linear finite elements with high accuracy*, J. Comput. Math., 3 (1985), pp. 115–133.

[20] L Lu, J D Joannopoulos, and M Soljačić, *Topological photonics*, Nature Photonics, 8 (2014), pp. 821–829.

[21] Ling Lu, John D Joannopoulos, and Marin Soljacic, *Topological states in photonic systems*, Nature Physics, 12 (2016), pp. 626–629.

[22] S H Mousavi, A B Khanikaev, and Z Wang, *Topologically protected elastic waves in phononic metamaterials*, Nature communications, 6 (2015).

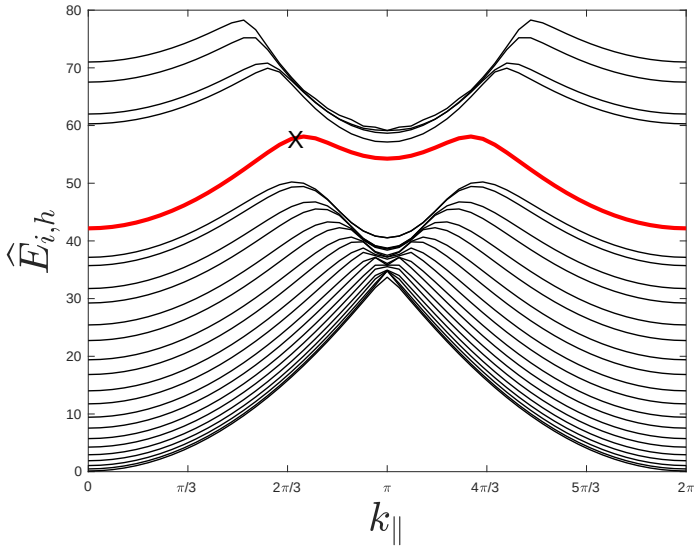

Fig. 4.7: Eigenvalues computed by gradient recovery methods for the $\mathcal{P}$-symmetry breaking case (4.6)-(4.7) with $L = 10$. The edge mode is corresponding to the line marked by 'X'.

[23] A. Naga and Z. Zhang, *A posteriori error estimates based on the polynomial preserving recovery*, SIAM J. Numer. Anal., 42 (2004), pp. 1780–1800 (electronic).

[24] ———, *The polynomial-preserving recovery for higher order finite element methods in 2D and 3D*, Discrete Contin. Dyn. Syst. Ser. B, 5 (2005), pp. 769–798.

[25] A. Naga, Z. Zhang, and A. Zhou, *Enhancing eigenvalue approximation by gradient recovery*, SIAM J. Sci. Comput., 28 (2006), pp. 1289–1300.

[26] O. Peleg, G. Bartal, B. Freedman, O. Manela, M. Segev, and D. N. Christodoulides, *Conical diffraction and gap solitons in honeycomb photonic lattices*, Phys. Rev. Lett., 98 (2007), p. 103901.

[27] M C Rechtsman, Y Plotnik, J M Zeuner, D Song, Z Chen, A Szameit, and M Segev, *Topological creation and destruction of edge states in photonic graphene*, Physical review letters, 111 (2013), p. 103901.

[28] A. Singha, M. Gibertini, B. Karmakar, S. Yuan, M. Polini, G. Vignale, M. I. Katsnelson, A. Pinczuk, L. N. Pfeiffer, K. W. West, and V. Pellegrini, *Two-dimensional mott-hubbard electrons in an artificial honeycomb lattice*, Science, 332 (2011), pp. 1176–1179.

[29] G. Strang and G. Fix, *An analysis of the finite element method*, Wellesley-Cambridge Press, Wellesley, MA, second ed., 2008.

[30] H. Wu and Z. Zhang, *Enhancing eigenvalue approximation by gradient recovery on adaptive meshes*, IMA J. Numer. Anal., 29 (2009), pp. 1008–1022.

[31] L.-H. Wu and X. Hu, *Scheme for achieving a topological photonic crystal by using dielectric material*, Physical review letters, 114 (2015), p. 223901.

[32] Z. Yang, F. Gao, X. Shi, X. Lin, Z. Gao, Y. Chong, and B. Zhang, *Topological acoustics*, Physical review letters, 114 (2015), p. 114301.

[33] Z. Zhang and A. Naga, *A new finite element gradient recovery method: superconvergence property*, SIAM J. Sci. Comput., 26 (2005), pp. 1192–1213 (electronic).

[34] O. C. Zienkiewicz and J. Z. Zhu, *A simple error estimator and adaptive procedure for practical engineering analysis*, Internat. J. Numer. Methods Engrg., 24 (1987), pp. 337–357.

[35] ———, *The superconvergent patch recovery and a posteriori error estimates. I. The recovery technique*, Internat. J. Numer. Methods Engrg., 33 (1992), pp. 1331–1364.

[36] ———, *The superconvergent patch recovery and a posteriori error estimates. II. Error estimates and adaptivity*, Internat. J. Numer. Methods Engrg., 33 (1992), pp. 1365–1382.

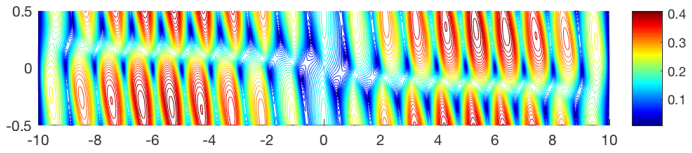

(a) The 19th eigenfunction

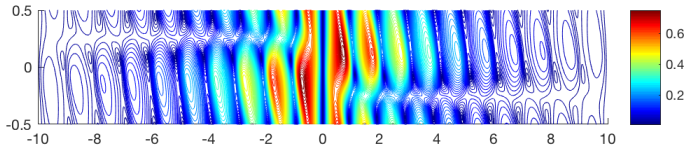

(b) The 20th eigenfunction

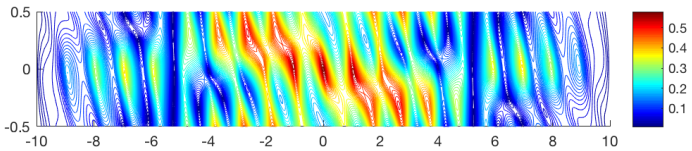

(c) The 21th eigenfunction

Fig. 4.8: Contour of the module of the eigenfunctions computed by gradient recovery method with $L = 10$ for the $\mathcal{P}$-symmetry breaking case (4.6)-(4.7) when $k_{\|} = \frac{2\pi}{3}$. We choose $\mathbf{v}_2$ as x-axis and $\mathbf{v}_1$ as y-axis. The 20th eigenfunction is the edge mode, which is periodic in $\mathbf{v}_1$ and localized at the center along $\mathbf{v}_2$.

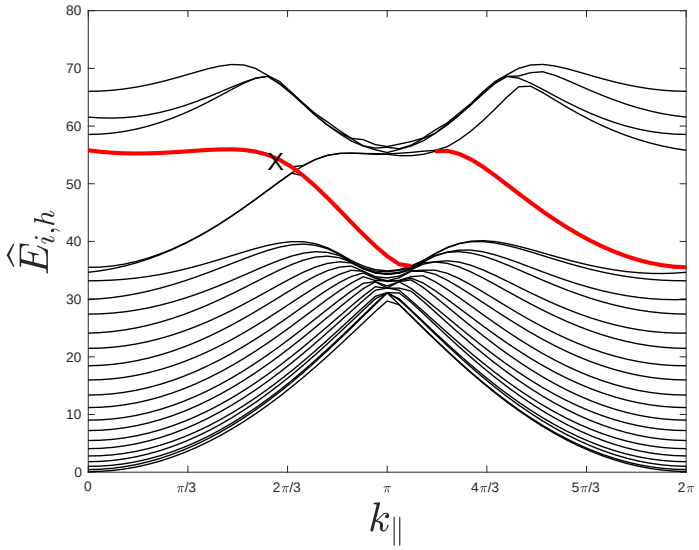

Fig. 4.9: Eigenvalues computed by gradient recovery methods for the $\mathcal{C}$-symmetry breaking case (4.8)-(4.9) with $L = 10$. The edge mode is corresponding to the line marked by 'X'.

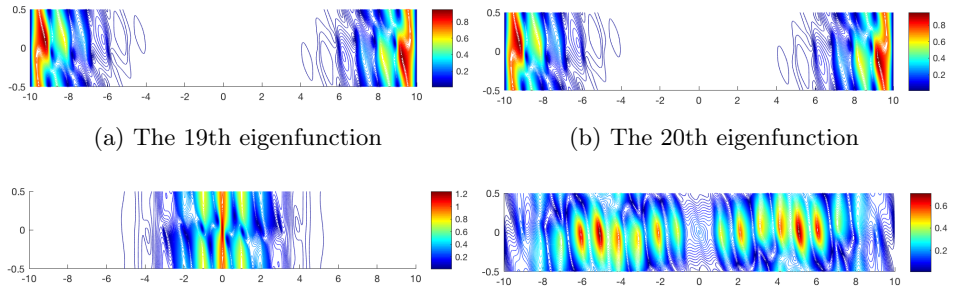

(a) The 19th eigenfunction

(b) The 20th eigenfunction

(c) The 21th eigenfunction

(d) The 22th eigenfunction

Fig. 4.10: Contour of the module of the eigenfunctions computed by gradient recovery method with $L = 10$ for the $\mathcal{C}$-symmetry breaking case (4.8)-(4.9) when $k_{\|} = \frac{2\pi}{3}$. We choose $\mathbf{v}_2$ as x-axis and $\mathbf{v}_1$ as y-axis. The 21th eigenfunction is the edge mode, which is periodic in $\mathbf{v}_1$ and localized at the center along $\mathbf{v}_2$.

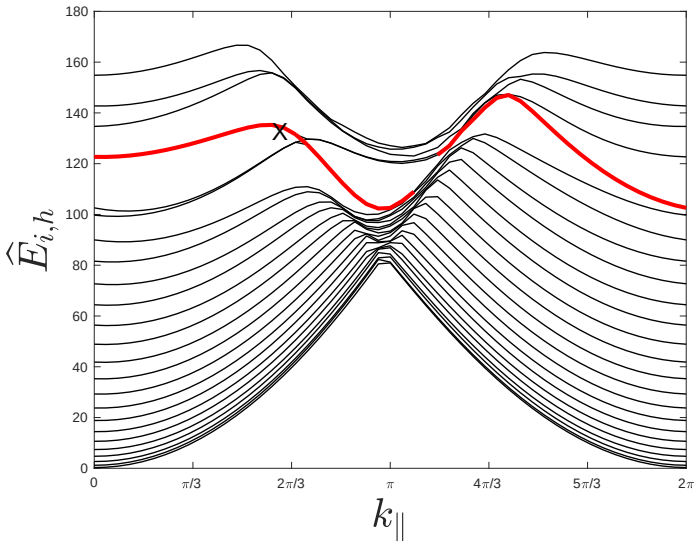

Fig. 4.11: Eigenvalues computed by gradient recovery methods for the anisotropic $\mathcal{C}$-symmetry breaking case (4.10)-(4.11) with $L = 10$. The edge mode is corresponding to the line marked by 'X'.

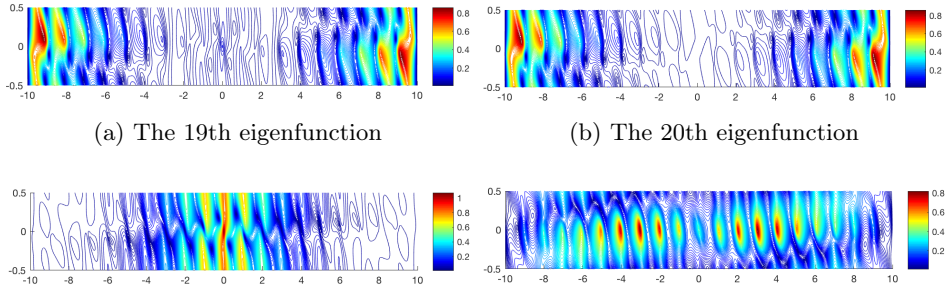

(a) The 19th eigenfunction

(b) The 20th eigenfunction

(c) The 21th eigenfunction

(d) The 22th eigenfunction

Fig. 4.12: Contour of the module of the eigenfunctions computed by gradient recovery method with $L = 10$ for the anisotropic $\mathcal{C}$-symmetry breaking case (4.10)-(4.11) when $k_{\|} = \frac{2\pi}{3}$. We choose $\mathbf{v}_2$ as x-axis and $\mathbf{v}_1$ as y-axis. The 21th eigenfunction is the edge mode, which is periodic in $\mathbf{v}_1$ and localized at the center along $\mathbf{v}_2$.